Weak Grid Operation of A Grid-Following Current-Sourced PV Solar System

Zhengyu Wang, Zhixin Miao, Lingling Fan, Amirnaser Yazdani

***Abstract*—A barrier to achieving high switching frequencies for the popular voltage-sourced inverter (VSI) topology is that the output voltage of a VSI is subject to significant changes instantaneously. The current-soured inverters (CSI) avoid such shortcoming and have been applied in grid-following inverters for photovoltaic (PV) solar. This paper presents the dynamic performance of a CSI grid-following PV solar operating with a weak grid. The simulation is carried out in MATLAB/Simulink with SimPowerSystems toolbox. The case study results illustrate the operation limits of a grid-following CSI and how those limits are associated with voltage stability and CSI's control settings.**

***Index Terms*—PV solar, current-sourced inverter (CSI), grid-following inverter.**

I. Introduction

INVERTER-based renewable energy resources, e.g., photovoltaics (PVs) solar, are installed world wide. A grid-connected inverter serves as the interface between a PV solar and the power grid.

Currently, the voltage-sourced inverter (VSI) is the most common inverter topology for PV integration. The advantages of the VSI include its simple structure, relatively low power losses, and voltage controllability. However, due to the nature of the VSI, the output voltage is subject to instantaneous changes and contains high-frequency harmonics. An alternative topology for converters, the current-sourced inverter (CSI), can avoid such shortcomings. Compared to a VSI, the capabilities of voltage-boosting and current controllability of the CSI are essential. As a recent paper on wide-bandgap power electronic devices [1] indicates, the newly designed power-electronic modules can significantly improve the power losses due to high switching frequency for the CSIs. Trending technology could make high-power CSIs become a strong alternative in the future. Additionally, the dc-dc converter that is necessary for the PV system connected to the VSI can be dispensed with the CSI being applied [2]–[4].

Although CSIs are capable of handling the interconnection of grid-tied PV systems, the low-order harmonics from a CSI's output current cannot be ignored. In turn, passive filters, usually CL filters, are necessary to handle the low-order harmonics [5]–[7].

As VSI-based systems have been studied by many textbooks and literature [8]–[11], the CSI-based system deserves an in-depth study and research. In this paper, operation of a CSI-based PV solar interconnected with a weak grid is investigated. An electromagnetic transient (EMT) simulation testbed is built based on the CSI module developed from [3] and implemented in MATLAB/Simulink-based SimPowerSystems environment. First, the modeling and control details are reviewed, including the PV array implementation, IGBT-based CSI structure, and current control of the grid-following CSI. Second, based on the testbed, a series of dynamic events are designed and simulated, such as weak grid connection, followed by the analysis of the dynamic performance.

The main contribution of this paper is the weak grid operation analysis of a grid-following CSI, which offers insights into the relationship between the operation limits and the control settings.

The rest of the paper is presented as follows. Section II presents the detailed implementation of the grid-following CSI-based PV testbed. The case studies developed based on the simulation testbed is presented in Section III. Section IV concludes the paper.

II. Grid-following CSI-based PV system

The study system is a grid-following CSI-based PV testbed as shown in Fig. 1. A 100-kW PV solar array provides DC power to the three-phase IGBT-based CSI. An inductor, L_{dc}, is installed to smooth the DC-side current flow. The AC-side filter is implemented with a shunt capacitor, C, a resistor, R, and an inductor, L. The point of common coupling (PCC) is on the bus after the inductor. A step-up transformer is placed at the PCC bus to boost the voltage to transmission level. An RL type of transmission line connects the transformer to the grid, represented by an infinite bus. The system parameters are shown in the Table I

TABLE I: Parameters of the EMT testbed

Category	Description	Parameter	Value
System	Rated Power	P_n	100 kW
	Rated Voltage	V_n	380 V, 20 kV
	Nominal Frequency	f_n	50 Hz
Passives	DC-side inductance	L_{dc}	5 mH
	Choke reactance	X	0.44 $p.u.$
	Choke resistance	R	0.14 $p.u.$
	Shunt capacitor susceptance	B_C	0.02 $p.u.$
	X/R ratio	X/R	10
	Line reactance	X_g	0.01 $p.u.$
Controller	Switching frequency	f_{sw}	2550 Hz
	DC current controller	$K_{p,dc}, K_{i,dc}$	-0.002, -0.02
	AC current controller	$K_{p,ac}, K_{i,ac}$	0, 500

The PV solar array assumed in this paper is based on the SunPower SPR-305E-WHT-D module. There are 66 parallel strings of PV panels, and each string has 5 modules connected in series. The rated power for each module is 305 W, and the total output power of the PV array is about 100 kW. The full

Z. Wang, Z. Miao, and L. Fan are with Electrical Engineering Dept., Univ. of South Florida. Email: linglingfan@usf.edu

A. Yazdani is with Ryerson University. Email: yazdani@ryerson.ca.

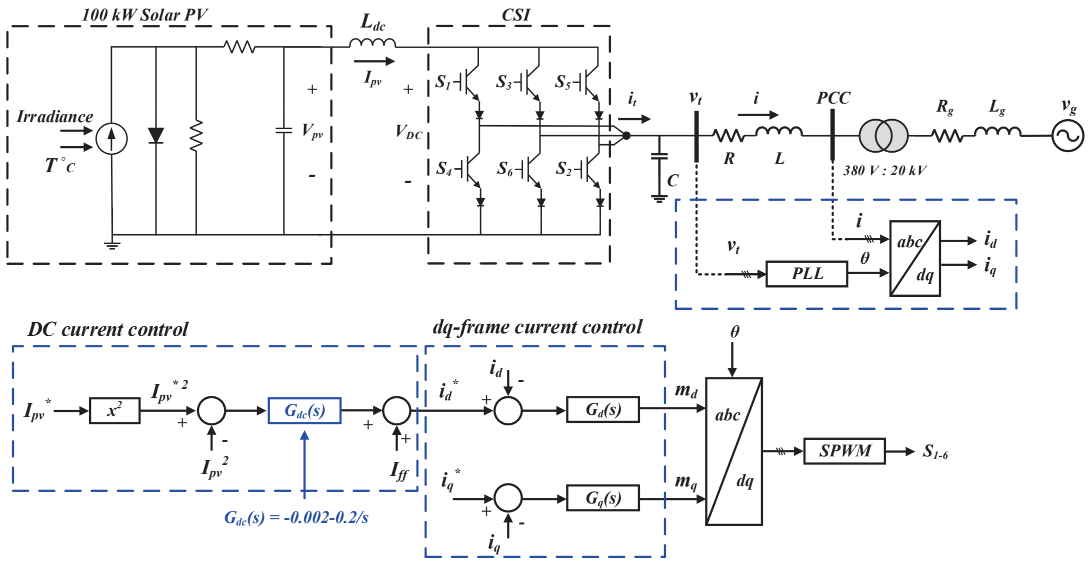

Fig. 1: Circuit topology and CSI control structure of a 100-kW grid-following CSI-based PV system.

TABLE II: Parameters of the EMT testbed

Parameter	Value
Parallel strings	66
Series-connected modules per string	5
Module maximum power	305 W
Cells per module (N_{cell})	96
Open-circuit voltage V_{oc}	64.2 V
Short-circuit current I_{sc}	5.96 A
Voltage at maximum power point V_{mp}	54.7
Current at maximum power point I_{mp}	5.58 A
Temperature coefficient of V_{oc}	$-0.27269°C$
Temperature coefficient of I_{sc}	$0.061745°C$

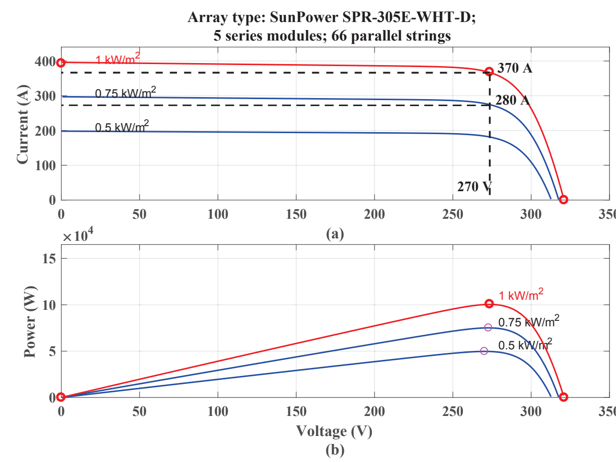

Fig. 2: I-V and P-V characteristics of SunPower SPR-305E-WHT-D. (a) I-V curve. (b) P-V curve. Maximum power of 100 kW occurs at $I_{pv} = 370$ A and $V_{pv} = 270$ V when sun irradiance is 1 kW/m^2.

specification of the PV array model is shown in Table II. The I-V and P-V characteristics of the implemented PV array are shown in Fig. 2. In the testbed, the temperature is fixed at 25 $°C$. The maximum power occurs at $I_{pv} = 370$ and 280 A and $V_{pv} = 270$ V when solar irradiance is 1 and 0.75 kW/m^2 respectively.

A three-phase IGBT-based CSI is employed to deliver the power from the PV solar array to the main power grid. Each converter switch consists of an IGBT and a series-connected diode [3] (Fig. 1).

Due to the switching, the terminal currents are pulsed as shown in Fig. 2(b), while the capacitor voltages, v_t, are close to sinusoidal waveforms with harmonics, as shown in Fig. 3(d). These are duals to the VSI's output voltages and currents.

The relationship between the DC side current I_{pv}, and terminal current i_t, is as follows [3], [4].

$$i_{ta,b,c} = m_{a,b,c} \cdot I_{pv}, \tag{1}$$

where $m_{a,b,c}$ signifies the modulation waveforms for phase a, b and c.

Fig. 3(a) presents how the modulation index impacts the terminal current. The magnitude of the modulation index is increased from 0.5 to 0.8, at 0.5 seconds, while the input current from PV is set constant at 280 A.

Fig. 3(b) shows that the peak value of the terminal current is 280 A. The fundamental frequency component's magnitude is shown tracking the modulation index's change.

For a grid-following system, the synchronization between the renewable energy resources and the power grid is important. A three-phase phase-locked loop (PLL) with automatic gain control and a moving average filter ("Variable Frequency Mean Value" block) [12] is applied to track the angle of terminal voltage, v_t, for reference frame change and Park's transformation of measurements. The PLL structure is shown in Fig. 4.

The CSI's control structure is shown in Fig. 1, where the outer control loop achieves DC current control, which regulates the PV's output dc current. The inner control loop is for AC current control and its reference frame is aligned to

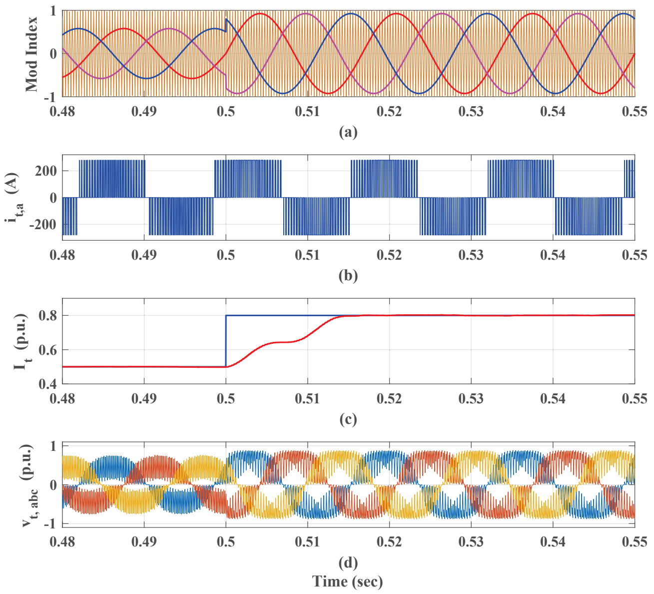

Fig. 3: CSI output response when the modulation index increases from 0.5 to 0.8 at 0.5 seconds: (a) modulation signal compared with carrier wave; (b) terminal current, $i_{t,a}$; (c) terminal current RMS value, I_t; and (d) terminal voltage fundamental frequency component, $v_{t,abc}$.

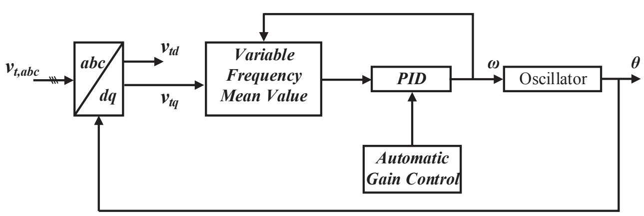

Fig. 4: The structure of the three-phase PLL.

the terminal voltage by use of the PLL output angle θ. The three-phase current is converted to dq-components using θ and fed into the inner AC current control scheme.

The input of the DC current control is the PV current reference, I_{pv}^*, and its output is the reference of d-axis AC current, i_d^*. The DC-side current dynamic is governed by

$$\frac{dI_{pv}}{dt} = \frac{1}{L_{dc}}(V_{pv} - V_{dc}), \tag{2}$$

where V_{pv} is the PV array's output voltage and V_{dc} is the DC voltage after DC-side inductor. By multiplying I_{pv} on both side, Eq. 2 take the form:

$$\frac{dI_{pv}^2}{dt} = \frac{2}{L_{dc}}(P_{pv} - P_{dc}). \tag{3}$$

On the controller's reference frame (which aligns with the terminal voltage at steady state), the real and reactive powers can be expressed as follows.

$$P = \frac{3}{2}v_{td}i_d, \quad Q = -\frac{3}{2}v_{td}i_q \tag{4}$$

If the power loss in the power electronics devices is negligible, P_{dc} is equal to the real power obtained in Eq. 4. Thus, we update the dynamic equation to the following [5].

$$\frac{dI_{pv}^2}{dt} = \frac{2}{L_{dc}}(P_{pv} - \frac{3}{2}v_{td}i_d) \tag{5}$$

The above model shows that to increase I_{pv}, we should decrease i_d. This is the reason that a negative sign is put before a PI controller for the DC current controller ($G_{dc}(s)$) in Fig. 1.

Additionally, to compensate for the nonlinear dependence of the control on P_{pv}, a feed-forward current, I_{ff}, is implemented$\left(I_{\text{ff}} = \frac{P_{pv}}{\frac{3}{2}v_{td}}.\right)$

The output of the DC current control, i_d^*, is then sent into the AC current controller. The dq-frame modulation signals, m_d and m_q, are computed and converted to a three-phase reference signal for PWM generation. The inverse Park's transformation with the PLL's output angle, θ, is used for the conversion.

III. Case Study

In this section, case studies are conducted on the simulation testbed to demonstrate the performance of the grid-following CSI-based PV system under different conditions.

A. DC current regulation

As Fig. 1 shows, the PV output current, I_{pv}, is controlled by the DC current controller while the q-axis component of PCC current order, i_q^*, remains zero. Due to the PV's maximum power point tracking mechanism, when the sun irradiance increases from 0.75 to 1 kW/m^2 and PV output current increases from 280 A to 370 A, the PV voltage is kept the same at 270 V and the maximum output power increases from 75 kW to 100 kW. With these changes scheduled at 0.5 seconds, the responses of the testbed are shown in Figs. 5-8. Fig. 5 presents the measurements of the PV output current, I_{pv}, voltage, V_{pv}, and power, P_{pv}.

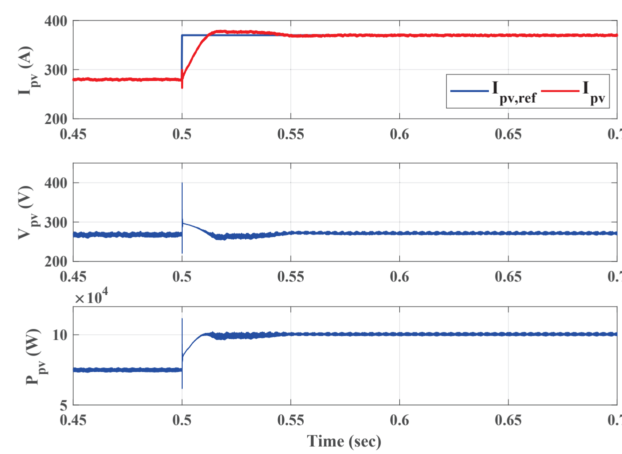

Fig. 5: Dynamic responses of I_{pv}, V_{pv}, and P_{pv} due to PV current reference increases at 0.5 seconds.

Inside the DC current controller, the responses of $G_{dc}(s)$ output, $I_{\text{pre}-I_{\text{ff}}}$, I_{ff}, and i_d^* are presented in Fig. 6. When DC current reference increases, the error is positive. The output of $G_{dc}(s)$ decreases, which is shown by Fig. 6(b). However, the irradiance increase causes I_{ff} to increase. The sum of the feedforward current and $G_{dc}(s)$ output is the current order I_d^*. This order is subject to a decrease in the initial stage and then an increase in the final stage.

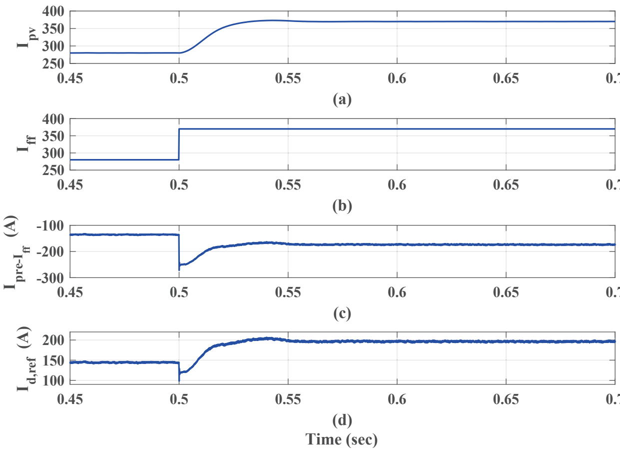

Fig. 6: DC current controller waveforms: (a) I_{pv}; (b) $I_{\text{pre}-\text{I}_{\text{ff}}}$; (c) I_{ff}; and (d) I_d^*

.

Due to the increased injected current and power, the AC side also experiences voltage, current, and power changes, correspondingly. The three-phase waveforms of the CSI terminal voltage, v_t, the voltage after filter, v_s, and the current through the PCC bus, i, are shown in Fig. 7.

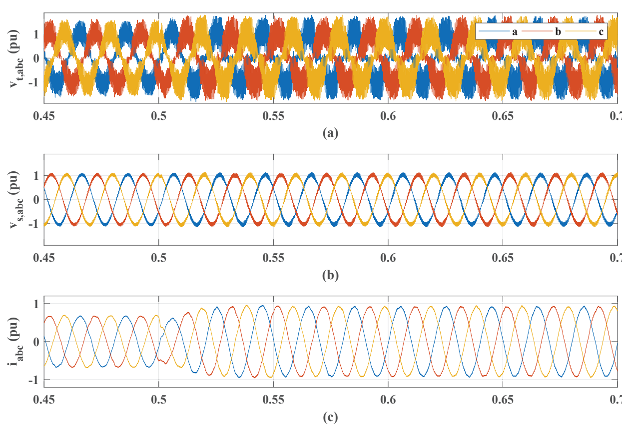

Fig. 7: Dynamic responses of three-phase v_t, v_{PCC}, and i.

Since the grid connection is strong, the voltage after the RL filter shows little impact from the event. However, the terminal voltage decreases in steady state, while the PCC bus current increases. Fig. 8 gives a clear presentation of magnitude changes of the filtered terminal voltage, current and power injected into the grid.

Remarks: The increase in real power injection causes the terminal voltage to decrease. This phenomenon is well known and associated with voltage stability. Due to the steady-state voltage stability limit, real power injection has a limit.

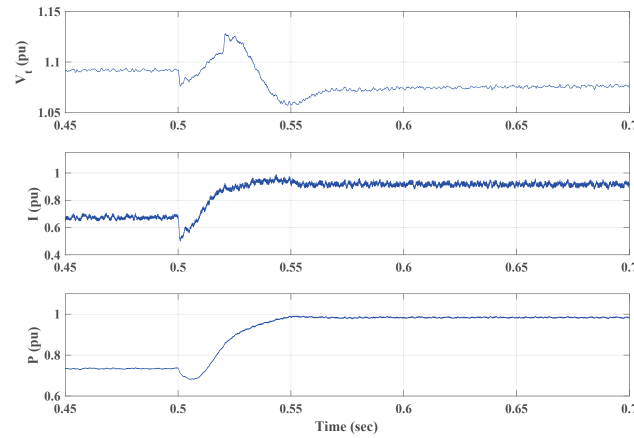

Fig. 8: Magnitudes of filtered terminal voltage, current and power injected to the grid.

B. Weak grid connection

When the grid impedance increases, the short circuit ratio (SCR) measured at the PCC bus decreases. This may cause the system to become unstable. In the testbed, a line tripping type of dynamic event is implemented to increase the grid impedance, X_g. The event details are as follows. The overall X/R ratio is kept at 10 and the PV output maximum power is kept at 75 kW.

- Grid impedance, X_g, increases from 0.35 to 0.375 p.u.
- Grid impedance, X_g, increases from 0.35 to 0.376 p.u.

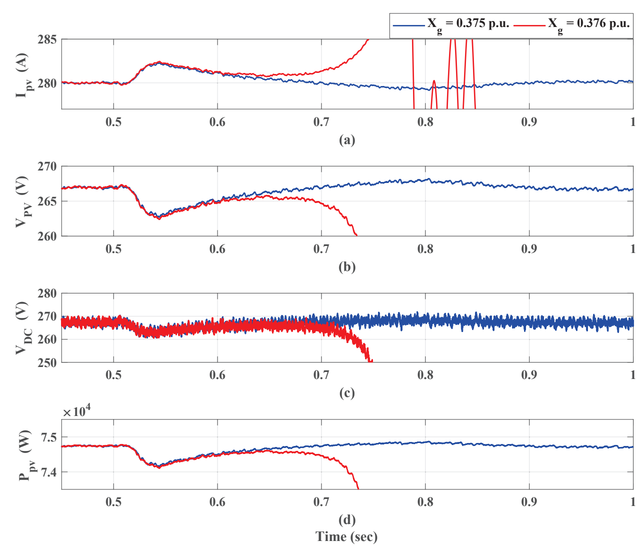

Fig. 9: DC side waveforms when grid impedance increases: (a) I_{pv}; (b) V_{pv}; (c) V_{DC}, and (d) P_{pv}. When X_g increases to 0.375 p.u., the system remains stable (Blue). When X_g increases to 0.376 p.u., the system becomes unstable.

The waveforms of I_{pv}, V_{pv}, V_{DC}, and P_{pv} are presented in Fig. 9 to show the DC side reaction to the line tripping event. Fig. 9 shows the CSI-based PV system remains stable when X_g increases to 0.375 p.u. but not to 0.376 p.u.

Next, the AC side waveforms are shown in Fig. 10, where the blue line indicates the stable case and the red line indicates the unstable case. The reactions of the PLL on its estimated frequency and identified phase angle are shown in Fig. 11.

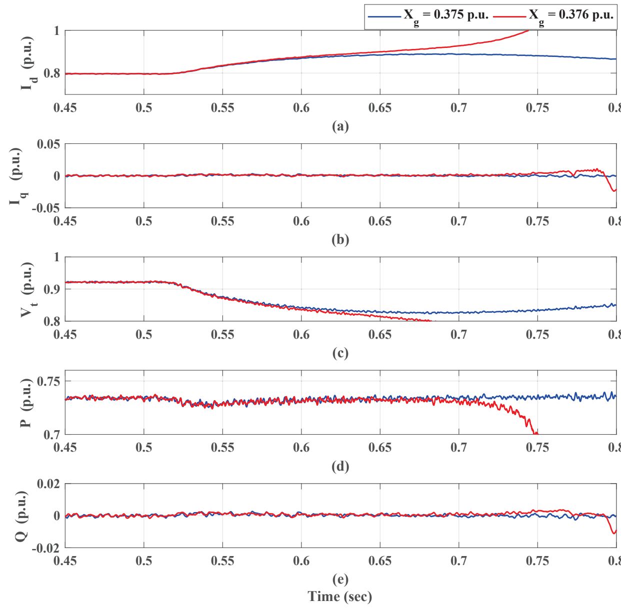

Fig. 10: AC side measurement when grid impedance increases: (a) i_d; (b) i_q; (c) V_t, (d) P; and (e) Q.

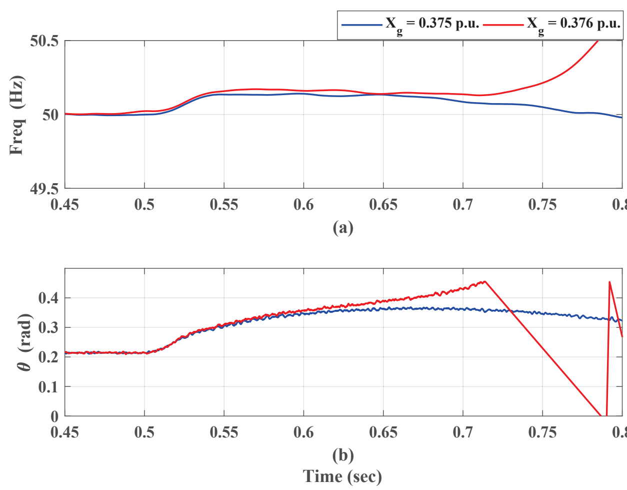

Fig. 11: PLL reaction to the grid impedance increases: (a) estimated frequency; (b) identified phase angle, θ.

According to the results shown in Figs. 9, 10, 11, it is be observed that the steady-state values of i_d and θ increase, whereas the voltage magnitude, V_t, decreases when the grid becomes weaker. The weak grid analysis is presented below.

A simplified circuit is shown below in Fig. 12. The reference frame is aligned with the terminal voltage. Thus, the terminal voltage phasor is $v_t = V_t\angle 0$ p.u. and the grid voltage phasor is $v_g = V_g\angle-\theta$. Assume the transmission line is expressed by a reactance, X_g.

When the line trips, X_g suddenly increases. The power balance equation for the circuit is: $P = \frac{V_t \cdot V_g}{X_g}\sin(\theta)$. Since the PV's output power is constant, the power injected into the grid is also constant. Assume that both bus voltage magnitudes are constant. To ensure constant P while X_g has increased, the angle difference shall increase. The angle increase is shown in Fig. 11(b).

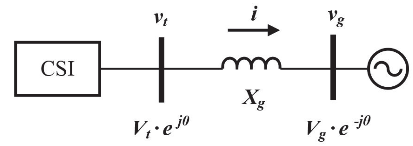

Fig. 12: Simplified circuit of the CSI-based PV system's grid side.

Further, assume that the grid voltage magnitude is kept at 1 p.u.. The terminal voltage can be expressed by the grid voltage and the current in the dq-frame that is aligned to v_t. Thus,

$$v_{td} + jv_{tq} = (i_d + ji_q)jX_g + (v_{gd} + jv_{gq}), \tag{6}$$

where $v_{gd} = \cos(\theta)$ and $v_{gq} = -\sin(\theta)$. Since the reference frame is aligned to the terminal voltage,

$$v_{td} = -i_q X_g + \cos(\theta) \tag{7}$$

$$v_{tq} = 0 = i_d X_g - \sin(\theta) \tag{8}$$

When θ increases, i_d also increases. On the other hand, $\cos(\theta)$ decreases, and v_{td} decreases. The dynamic responses in Fig. 10 corroborate the analysis. As the grid becomes weaker, the terminal voltage magnitude decreases. And the system stability is weakened due to the low voltage at the terminal.

From the relationship analyzed above, a strategy to improve the stability margin due to a weak grid is obtained. As we decrease the i_q^* to a negative value, v_{td} in steady state may drop less so that the system can handle a more weakened grid.

Remarks: When the grid has transmission line tripping and becomes weak, the CSI will experience an immediate increase in the DC-link current, a decrease in its AC side voltage and an increase in its AC side current. In addition, there is an operation limit, or voltage stability limit. Increasing reactive power injection from the converter may improve the operation limit.

IV. Conclusion

This paper presents the detailed modeling and control of grid-following CSI-based PV system, and the system's dynamic performance under weak grid conditions. The CSI's performance in transients and steady-state are examined and analyzed using a dynamic model for the PV system and a steady-state system model. The analysis agrees with the simulation results.

References

[1] T. M. Jahns and B. Sarlioglu, "The incredible shrinking motor drive: Accelerating the transition to integrated motor drives," *IEEE Power Electronics Magazine*, vol. 7, no. 3, pp. 18–27, 2020.

[2] S. A. Azmi, K. H. Ahmed, S. J. Finney, and B. W. Williams, "Comparative analysis between voltage and current source inverters in grid-connected application," in *IET Conference on Renewable Power Generation (RPG 2011)*, 2011, pp. 1–6.

[3] M. A. Azghandi, S. M. Barakati, and A. Yazdani, "Impedance-based stability analysis and design of a fractional-order active damper for grid-connected current-source inverters," *IEEE Transactions on Sustainable Energy*, 2020.

[4] Dong Shen and P. W. Lehn, "Modeling, analysis, and control of a current source inverter-based statcom," *IEEE Transactions on Power Delivery*, vol. 17, no. 1, pp. 248–253, 2002.

[5] P. P. Dash and M. Kazerani, “Dynamic modeling and performance analysis of a grid-connected current-source inverter-based photovoltaic system,” *IEEE Transactions on Sustainable Energy*, vol. 2, no. 4, pp. 443–450, 2011.

[6] A. A. A. Radwan and Y. A.-R. I. Mohamed, “Power synchronization control for grid-connected current-source inverter-based photovoltaic systems,” *IEEE Transactions on Energy Conversion*, vol. 31, no. 3, pp. 1023–1036, 2016.

[7] A. A. A. Radwan and Y. A. I. Mohamed, “Analysis and active suppression of ac- and dc-side instabilities in grid-connected current-source converter-based photovoltaic system,” *IEEE Transactions on Sustainable Energy*, vol. 4, no. 3, pp. 630–642, 2013.

[8] L. Fan, *Control and dynamics in power systems and microgrids*. CRC Press, 2017.

[9] J. Rocabert, A. Luna, F. Blaabjerg, and P. Rodriguez, “Control of power converters in ac microgrids,” *IEEE transactions on power electronics*, vol. 27, no. 11, pp. 4734–4749, 2012.

[10] A. Yazdani and R. Iravani, *Voltage-sourced converters in power systems: modeling, control, and applications*. John Wiley & Sons, 2010.

[11] N. Mohan, T. M. Undeland, and W. P. Robbins, *Power electronics: converters, applications, and design*. John wiley & sons, 2003.

[12] D. Jovcic, “Phase locked loop system for facts,” *IEEE transactions on power systems*, vol. 18, no. 3, pp. 1116–1124, 2003.